Constrained Synthesis with Projected Diffusion Models

Jacob K Christopher
University of Virginia
csk4sr@virginia.edu

Stephen Baek
University of Virginia
baek@virginia.edu

Ferdinando Fioretto
University of Virginia
fioretto@virginia.edu

Abstract

This paper presents a novel approach that enhances generative diffusion models by enforcing compliance with specified constraints and physical principles. We reformulate the traditional sampling process used in these models into a constrained optimization problem. This reformulation guides the generated data to adhere closely to predefined boundaries, thereby ensuring the models comply with relevant constraints. Our methodology is demonstrated across various applications, including the generation of new materials with targeted morphometric characteristics, the synthesis of physics-informed motion, optimized path planning, and the creation of realistic human motion.

1 Introduction

Generative diffusion models excel at robustly synthesizing content from raw noise through a sequential denoising process [14, 24]. They have revolutionized high-fidelity creation of complex data, and their applications have rapidly expanded beyond mere image synthesis, finding relevance in areas such as engineering [29, 34], automation [3, 16], chemistry [1, 15], and medical analysis [2, 6]. Although diffusion models excel at generating content that is coherent and aligns closely with the original data distribution, their direct application in scenarios requiring stringent adherence to predefined criteria poses significant challenges. Particularly the use of diffusion models in domains where the generated data needs to not only resemble real-world examples but also rigorously comply with established specifications and physical laws remains an open challenge. This paper addresses these challenges and introduces *Projected Diffusion Models* (PDM), a novel approach that recast the traditional sampling strategy in diffusion processes as a constrained-optimization problem. In this work, the problem is solved by iteratively projecting the diffusion sampling process onto arbitrary constraint sets, ensuring that the generated data adheres strictly to imposed constraints or physical principles. This alignment is a significant advantage of PDM, yielding state-of-the-art FID scores while maintaining strict compliance with the imposed constraints.

2 Related work and limitations

Model conditioning [13] aims to control generation by augmenting the diffusion process via a conditioning variable $\boldsymbol{c}$ to transform the denoising process.These methods are effective in capturing properties of physical design [29], positional awareness [3], and motion dynamics [32]. However, while conditioning may be effective to influence the generation process, it lacks the rigor to ensure adherence to specific constraints. This results in generated outputs that, despite being plausible, may not be accurate or reliable. Figure 1 (red colors) illustrates this issue on a physics-informed motion experiment (detailed in §4.3).

Machine Learning and the Physical Sciences Workshop, NeurIPS 2024.

Post-processing correction. An alternative approach involves applying post-processing steps to correct deviations from desired constraints in the generated samples. This correction is typically implemented in the last noise removal stage, $s_\theta(\boldsymbol{x}_1, 1)$. Some approaches have augmented this process to use optimization solvers to impose constraints on synthesized samples [10, 19, 21]. However these approaches present two main limitations. First, their objective does not align with optimizing the score function. This inherently positions the diffusion model's role as ancillary, with the final synthesized data often resulting in a significant divergence from the learned (and original) data distributions, as we will demonstrate in §4. Second, these methods are reliant on a limited and problem specific class of objectives and constraints, such as specific trajectory "constraints" or shortest path objectives which can be integrated as a post-processing step [10, 21].

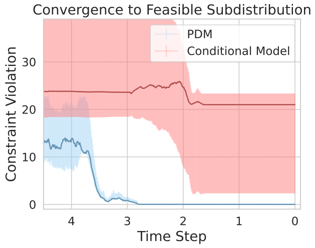

Figure 1: Sampling steps failing to converge to feasible solutions in conditional models (red) while minimizing the constraint divergence to 0 under PDM (blue).

3 Constrained generative diffusion

This section establishes a theoretical framework that connects the reverse diffusion process as an optimization problem. This perspective facilitates the incorporation of constraints directly into the process, resulting in the constrained optimization formulation presented in Equation (4).

The application of the reverse diffusion process of score-based models is characterized by iteratively transforming the initial noisy samples $\boldsymbol{x}_T$ back to a data sample $\boldsymbol{x}_0$ following the learned data distribution $q(\boldsymbol{x}_0)$. This transformation is achieved by iteratively updating the sample using the estimated score function $\nabla_{\boldsymbol{x}_t} \log q(\boldsymbol{x}_t|\boldsymbol{x}_0)$, where $q(\boldsymbol{x}_t|\boldsymbol{x}_0)$ is the data distribution at time t. At each time step t, starting from $\boldsymbol{x}_t^0$, the process performs M iterations of *Stochastic Gradient Langevin Dynamics* (SGLD) [30]:

$$\boldsymbol{x}_t^{i+1} = \boldsymbol{x}_t^i + \gamma_t \nabla_{\boldsymbol{x}_t^i} \log q(\boldsymbol{x}_t^i|\boldsymbol{x}_0) + \sqrt{2\gamma_t}\boldsymbol{\epsilon}, \tag{1}$$

where $\boldsymbol{\epsilon}$ is standard normal, $\gamma_t > 0$ is the step size, and $\nabla_{\boldsymbol{x}_t^i} \log q(\boldsymbol{x}_t^i|\boldsymbol{x}_0)$ is approximated by the learned score function $\mathbf{s}_\theta(\mathbf{x}_t, t)$.

3.1 Casting the reverse process as an optimization problem

First note that SGLD is derived from discretizing the continuous-time Langevin dynamics, which are governed by the stochastic differential equation:

$$d\boldsymbol{X}(t) = \nabla \log q(\boldsymbol{X}(t))\, dt + \sqrt{2}\, d\boldsymbol{B}(t), \tag{2}$$

where $\boldsymbol{B}(t)$ is standard Brownian motion. Under appropriate conditions, the stationary distribution of this process is $q(\boldsymbol{x}_t)$ [22], implying that samples generated by Langevin dynamics will, over time, be distributed according to $q(\boldsymbol{x}_t)$. In practice, these dynamics are simulated using a discrete-time approximation, leading to the SGLD update in Equation (1). Therein the noise term $\sqrt{2\gamma_t}\,\boldsymbol{\epsilon}_t^i$ allows the algorithm to explore the probability landscape and avoid becoming trapped in local maxima.

Next notice that, as detailed in [30, 31], under some regularity conditions this iterative SGLD algorithm converges toward a stationary point, bounded by $\frac{d^2}{\sigma^{1/4}\lambda^*} \log(1/\epsilon)$, where, σ^2 represents the variance schedule, λ^* denotes the uniform spectral gap of the Langevin diffusion, and d is the dimensionality of the problem. Thus, as the reverse diffusion process progresses towards $T \to 0$, and the variance schedule decreases, the stochastic component becomes negligible, and SGLD transitions toward deterministic gradient ascent on $\log q(\boldsymbol{x}_t)$. In the limit of vanishing noise, the update rule simplifies to:

$$\boldsymbol{x}_t^{i+1} = \boldsymbol{x}_t^i + \gamma_t \nabla_{\boldsymbol{x}} \log q(\boldsymbol{x}_t^i|\boldsymbol{x}_0), \tag{3}$$

which is standard gradient ascent aiming to maximize $\log q(\boldsymbol{x}_t)$. This allow us to view the reverse diffusion process as an optimization problem minimizing the negative log-likelihood of the data distribution $q(\boldsymbol{x}_t|\boldsymbol{x}_0)$ at each time step t.

In traditional score-based models, at any point throughout the reverse process, $\boldsymbol{x}_t$ is *unconstrained*. When these samples are required to satisfy some constraints, the objective remains unchanged, but the solution to this optimization must fall within a feasible region $\mathbf{C}$, and thus the optimization problem formulation becomes:

$$\underset{\boldsymbol{x}_T,\dots,\boldsymbol{x}_1}{\text{minimize}} \sum_{t=T,\dots,1} -\log q(\boldsymbol{x}_t|\boldsymbol{x}_0) \tag{4a}$$

$$\text{s.t.:} \quad \boldsymbol{x}_T,\dots,\boldsymbol{x}_0 \in \mathbf{C}. \tag{4b}$$

Operationally, the negative log likelihood is minimized at each step of the reverse Markov chain, as the process transitions from $\boldsymbol{x}_T$ to $\boldsymbol{x}_0$. In this regard, and importantly, the objective of the PDM's reverse sampling process is aligned with that of traditional score-based diffusion models.

3.2 Constrained guidance through iterative projections

The score network $\mathbf{s}_\theta(\boldsymbol{x}_t, t)$ directly estimates the first-order derivatives of Equation (4a), providing the necessary gradients for iterative gradient-based updates defined in Equation (1). In the presence of constraints (4b), however, an alternative iterative method is necessary to guarantee feasibility. PDM models a projected guidance approach to provide this constraint-aware optimization process.

First, we define the projection operator, $\mathcal{P}_\mathbf{C}$, as a constrained optimization problem,

$$\mathcal{P}_\mathbf{C}(\boldsymbol{x}) = \underset{\boldsymbol{y}\in\mathbf{C}}{\text{argmin}}\, ||\boldsymbol{y}-\boldsymbol{x}||_2^2, \tag{5}$$

that finds the nearest feasible point to the input $\boldsymbol{x}$. The *cost of the projection* $||\boldsymbol{y}-\boldsymbol{x}||_2^2$ represents the distance between the closest feasible point and the original input.

To retain feasibility through an application of the projection operator after each update step, the paper defines *projected diffusion model sampling* step as

$$\boldsymbol{x}_t^{i+1} = \mathcal{P}_\mathbf{C}\left(\boldsymbol{x}_t^i + \gamma_t \nabla_{\boldsymbol{x}_t^i} \log q(\boldsymbol{x}_t|\boldsymbol{x}_0) + \sqrt{2\gamma_t}\boldsymbol{\epsilon}\right), \tag{6}$$

where $\mathbf{C}$ is the set of constraints and $\mathcal{P}_\mathbf{C}$ is a projection onto $\mathbf{C}$. Hence, iteratively throughout the Markov chain, a gradient step is taken to minimize the objective defined by Equation (4a) while ensuring feasibility. Convergence is guaranteed for convex constraints sets [20] and empirical evidence in §4 showcases the applicability of this methods to arbitrary constraint sets. Importantly, the projection operators can be *warm-started* during the repeated sampling step providing a piratical solution even for hard non-convex constrained regions. The full sampling process is detailed in Algorithm 1.

By incorporating constraints throughout the sampling process, the interim learned distributions are steered to comply with these specifications. This is empirically evident from the pattern in Figure 1 (blue curves): remarkably, the constraint violations decrease with each addition of estimated gradients and noise and approaches 0-violation as t nears zero. *This trend not only minimizes the impact but also reduces the optimality cost of projections applied in the later stages of the reverse process.* We provide theoretical rationale for the effectiveness of this approach in §D and conclude this section by noting that this approach can be clearly distinguished from other methods which use a diffusion model's sampling process to generate starting points for a constrained optimization algorithm [10, 21]. Instead, PDM leverages minimization of negative log likelihood as the primary objective of the sampling algorithm akin to standard unconstrained sampling procedures. This strategy offers a key advantage: *the probability of generating a sample that conforms to the data distribution is*

Algorithm 1: PDM

```
$\boldsymbol{x}_T^0 \sim \mathcal{N}(\mathbf{0}, \sigma_T \boldsymbol{I})$
for $t = T$ to $1$ do
    $\gamma_t \leftarrow \sigma_t^2 / 2\sigma_T^2$
    for $i = 1$ to $M$ do
        $\boldsymbol{\epsilon} \sim \mathcal{N}(\mathbf{0}, \boldsymbol{I})$;   $\boldsymbol{g} \leftarrow \boldsymbol{s}_{\theta^*}(\boldsymbol{x}_t^{i-1}, t)$
        $\boldsymbol{x}_t^i = \mathcal{P}_{\boldsymbol{C}}(\boldsymbol{x}_t^{i-1} + \gamma_t \boldsymbol{g} + \sqrt{2\gamma_t}\boldsymbol{\epsilon})$
    $\boldsymbol{x}_{t-1}^0 \leftarrow \boldsymbol{x}_t^M$
return $\boldsymbol{x}_0^0$
```

optimized directly, rather than an external objective, *while simultaneously imposing verifiable constraints*. In contrast, existing baselines often neglect the conformity to the data distribution, which, as we will show in the next section, can lead to a deviation from the learned distribution and an overemphasis on external objectives for solution generation, resulting in significant divergence from the data distribution, reflected by high FID scores.

4 Experiments

We compare PDM against three methodologies, each employing state-of-the-art specialized methods tailored to the various applications tested:: **(1)** *Conditional diffusion models* (*Cond*) [13] are the state-of-the-art methods for generative sampling subject to a series of specifications. While conditional diffusion models offer a way to guide the generation process towards satisfying certain constraints, they do not provide compliance guarantees. **(2)** To encourage constraints satisfaction, we additionally compare to conditional models with a post-processing projection step (*Cond*$^{+}$), emulating the post-processing approaches of [10, 21] in various domains presented next. Finally, **(3)** we use a score-based model identical to our implementation but with a single post-processing projection operation (*Post*$^{+}$) performed at the last sampling step. The performance of these models are evaluated by the *feasibility* and *accuracy* of the generated samples. Additional details and results are provided in Sections E and F.

4.1 Constrained materials *(low data regimes and constraint-violating distributions)*

The first setting focuses on a *real-world* application in material science, conducted as part of an experiment to expedite the discovery of structure-property linkages (please see §F for extensive additional details). From a sparse collection of microstructure materials, we aim to generate new structures with desired, previously unobserved porosity levels.

There are two key challenges in this setting: **(1) Data sparsity:** A critical factor in this setting is the cost of producing training data. Our dataset consists of 64×64 image patches subsampled from a $3,000 \times 3,000$ pixel microscopic image, with pixel values scaled to $[-1, 1]$. These patches are upscaled to 256×256 for training. **(2) Out-of-distribution constraints:** Constraints on the generated material's porosity are far from those observed in the original dataset.

Ground	P(%)	Generative Methods			
		PDM	*Cond*	*Post*$^{+}$	*Cond*$^{+}$
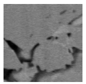	30	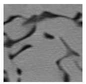	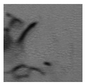	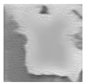	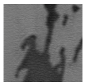
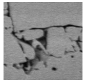	50	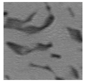	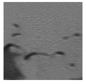	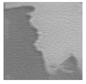	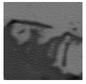
FID scores:		**30.7±6.8**	31.7±15.6	41.7±12.8	46.4±10.7

Figure 2: Microstructure visualization at varying of the imposed porosity constraint amounts (P).

Previous work has failed to impose verifiable constraints on desired properties [5, 11]. We implement a conditional diffusion model (*Cond*), following the state-of-the-art approach by [5], conditioning the sampling on porosity measurements. This state-of-the-art model struggles to adhere to the constraints, *producing infeasible solutions 90% of the time with a generous error tolerance of 10% porosity* (Figure 9). In contrast, PDM ensures both *exact* constraint satisfaction and identical image quality to the conditional model. Additionally, we find that PDM outperforms *Cond* in generating microstructures that resemble those in the ground truth data **(see §E.1)**. *These results are significant: the ability to precisely control morphological parameters in synthetic microstructures has broad impact in material synthesis, addressing critical challenges in data collection and property specification.*

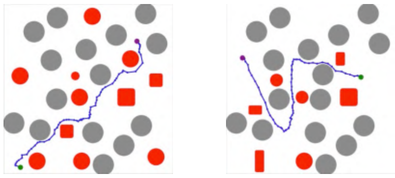

Figure 3: Constrained trajecotires synthetized by PDM on two topographies (Tp1, left and Tp2, right).

		PDM	*Cond* (MPD) [3]	*Cond*$^{+}$
S	Tp 1	**100.0 ± 0.0**	77.1 ± 29.2	77.1 ± 29.2
	Tp 2	**100.0 ± 0.0**	53.3 ± 35.7	53.3 ± 35.7
PL	Tp 1	2.21 ± 0.26	2.08 ± 0.51	2.08 ± 0.51
	Tp 2	2.05 ± 0.17	2.09 ± 0.31	2.09 ± 0.31

Figure 4: Constrained trajectories evaluation on success percentage (**S**) for a single run (higher the better, top) and path length, **PL**, (lower the better, bottom).

4.2 Constrained trajectories (*nonconvex constraints*)

The next experiment showcase the ability of PDM to handle nonconvex constraints. Path planning is a classic optimization problem which is integral to finding smooth, collision-free paths in autonomous systems. [3]. In this task, the diffusion model predicts a series of points, $p_0, p_1, \ldots, p_N$, where each pair of consecutive points represents a line segment. The problem presents obstacles at inference time (shown in red on Figure 3), rendering a portion of the training data infeasible, and thus testing the generalization of these methods. The performance is evaluated on two sets of maps adapted from [3], shown in Figure 3. The main challenge in this setting is the **non-convex nature of the constraints**.

Figure 3 visually demonstrates that PDM can identify a feasible path with just a single sample. This capability marks a significant advance over existing state-of-the-art motion planning methods with diffusion models, as it eliminates the necessity of multiple inference attempts, which greatly affects the efficiency in generating feasible solutions. The experimental results (Figure 4) demonstrate the effectiveness of PDM in handling complex, non-convex constraints in terms of success percentage for single trajectories generated (top) and path length (bottom). Frequently both the *Cond* and *Cond*$^+$ models fall short in finding feasible trajectories, taking shortcuts resulting in collisions. *These results are significant: they show that PDM can not only handle complex, non-convex constraints, but also produce results that are on par with state-of-the-art models in solution optimality.*

4.3 Physics-informed motion *(ODEs and out-of-distribution constraints)*

Finally, we demonstrate PDM in generating video frames adhering to physical principles. The goal is to generate frames depicting an object accelerating due to gravity. The object's position in a given frame is governed by

$$\mathbf{p}_t = \mathbf{p}_{t-1} + \left(\mathbf{v}_t + \left(0.5 \times \frac{\partial \boldsymbol{v}_t}{\partial t}\right)\right), \tag{7a}$$

$$\mathbf{v}_{t+1} = \frac{\partial \boldsymbol{p}_t}{\partial t} + \frac{\partial \boldsymbol{v}_t}{\partial t} \tag{7b}$$

where $\mathbf{p}$ is the object position, $\mathbf{v}$ is the velocity, and t is the frame number. This positional information can be directly integrated into the constraint set of *PDM*, with constraint violations quantified by the pixel distance from their true position. In our experiment, the training data is based *solely* on earth's gravity and we test the model to simulate gravitational forces from the moon and other planets, in addition to earth. Thus there are two challenges in this setting **(1) satifying ODEs** describing our physical principle and **(2) generalize to out-of-distribution constraints**.

Figure 11 (left) shows randomly selected generated samples, with ground-truth images provided for reference. Samples generated by conditional diffusion models are not directly shown in the figure, as the white object outline in the *Cond*$^+$ frames shows where the *Cond* model originally positioned the object. *Post*$^+$ and *Cond*$^+$ show inaccuracies in the conditional model's object positioning, as indicated by the white outline in the 3rd and 4th columns (and graphically in Figure 10). Notably, this approach fails to produce *any viable sample within a zero-tolerance error margin*. In contrast, PDM generates frames that exactly satisfy the positional constraints, with FID scores comparable to those of *Cond*. Next, Figure 11 (right) shows the behavior of the models in settings where the training data does not include any feasible data points, adjusting the governing equation (7) to reflect the moon's gravitational pull. *PDM can handle complex governing equations (ODEs) and can guarantee satisfaction of out-of-distribution constraints with no decrease in sample quality.*

5 Conclusions

This paper was motivated by a significant challenge in the application of diffusion models in contexts requiring strict adherence to constraints and physical principles. It presented Projected Diffusion Models (PDM), an approach that recasts the score-based diffusion sampling process as a constrained optimization process that can be solved via the application of repeated projections. Experiments in domains ranging from physical-informed motion for video generation governed by ordinary differentiable equations, trajectory optimization in motion planning, and adherence to morphometric properties in generative material science processes illustrate the ability of PDM to generate content of high-fidelity that also adheres to complex non-convex constraints as well as physical principles.

References

[1] Namrata Anand and Tudor Achim. Protein structure and sequence generation with equivariant denoising diffusion probabilistic models. *arXiv preprint arXiv:2205.15019*, 2022.

[2] Chentao Cao, Zhuo-Xu Cui, Yue Wang, Shaonan Liu, Taijin Chen, Hairong Zheng, Dong Liang, and Yanjie Zhu. High-frequency space diffusion model for accelerated mri. *IEEE Transactions on Medical Imaging*, 2024.

[3] Joao Carvalho, An T Le, Mark Baierl, Dorothea Koert, and Jan Peters. Motion planning diffusion: Learning and planning of robot motions with diffusion models. In *2023 IEEE/RSJ International Conference on Intelligent Robots and Systems (IROS)*, pages 1916–1923. IEEE, 2023.

[4] Joseph B. Choi, Phong C. H. Nguyen, Oishik Sen, H. S. Udaykumar, and Stephen Baek. Artificial intelligence approaches for energetic materials by design: State of the art, challenges, and future directions. *Propellants, Explosives, Pyrotechnics*, 2023. doi: 10.1002/prep.202200276. URL `https://onlinelibrary.wiley.com/doi/full/10.1002/prep.202200276`.

[5] Sehyun Chun, Sidhartha Roy, Yen Thi Nguyen, Joseph B Choi, HS Udaykumar, and Stephen S Baek. Deep learning for synthetic microstructure generation in a materials-by-design framework for heterogeneous energetic materials. *Scientific reports*, 10(1):13307, 2020.

[6] Hyungjin Chung and Jong Chul Ye. Score-based diffusion models for accelerated mri. *Medical image analysis*, 80:102479, 2022.

[7] Nic Fishman, Leo Klarner, Valentin De Bortoli, Emile Mathieu, and Michael Hutchinson. Diffusion models for constrained domains. *arXiv preprint arXiv:2304.05364*, 2023.

[8] Nic Fishman, Leo Klarner, Emile Mathieu, Michael Hutchinson, and Valentin De Bortoli. Metropolis sampling for constrained diffusion models. *Advances in Neural Information Processing Systems*, 36, 2024.

[9] Thomas Frerix, Matthias Nießner, and Daniel Cremers. Homogeneous linear inequality constraints for neural network activations. In *Proceedings of the IEEE/CVF Conference on Computer Vision and Pattern Recognition Workshops*, pages 748–749, 2020.

[10] Giorgio Giannone, Akash Srivastava, Ole Winther, and Faez Ahmed. Aligning optimization trajectories with diffusion models for constrained design generation. *arXiv preprint arXiv:2305.18470*, 2023.

[11] Ian J Goodfellow, Jean Pouget-Abadie, Mehdi Mirza, Bing Xu, David Warde-Farley, Sherjil Ozair, Aaron Courville, and Yoshua Bengio. Generative adversarial nets. In *Advances in neural information processing systems*, pages 2672–2680, 2014.

[12] Chuan Guo, Shihao Zou, Xinxin Zuo, Sen Wang, Wei Ji, Xingyu Li, and Li Cheng. Generating diverse and natural 3d human motions from text. In *Proceedings of the IEEE/CVF Conference on Computer Vision and Pattern Recognition*, pages 5152–5161, 2022.

[13] Jonathan Ho and Tim Salimans. Classifier-free diffusion guidance. *arXiv preprint arXiv:2207.12598*, 2022.

[14] Jonathan Ho, Ajay Jain, and Pieter Abbeel. Denoising diffusion probabilistic models. *Advances in neural information processing systems*, 33:6840–6851, 2020.

[15] Emiel Hoogeboom, Vıctor Garcia Satorras, Clément Vignac, and Max Welling. Equivariant diffusion for molecule generation in 3d. In *International conference on machine learning*, pages 8867–8887. PMLR, 2022.

[16] Michael Janner, Yilun Du, Joshua B Tenenbaum, and Sergey Levine. Planning with diffusion for flexible behavior synthesis. *arXiv preprint arXiv:2205.09991*, 2022.

[17] Guan-Horng Liu, Tianrong Chen, Evangelos Theodorou, and Molei Tao. Mirror diffusion models for constrained and watermarked generation. *Advances in Neural Information Processing Systems*, 36, 2024.

[18] Aaron Lou and Stefano Ermon. Reflected diffusion models. In *International Conference on Machine Learning*, pages 22675–22701. PMLR, 2023.

[19] François Mazé and Faez Ahmed. Diffusion models beat gans on topology optimization. In *Proceedings of the AAAI Conference on Artificial Intelligence (AAAI), Washington, DC*, 2023.

[20] Neal Parikh and Stephen Boyd. Proximal algorithms. *Foundations and Trends in Optimization*, 1(3):127–239, 2014.

[21] Thomas Power, Rana Soltani-Zarrin, Soshi Iba, and Dmitry Berenson. Sampling constrained trajectories using composable diffusion models. In *IROS 2023 Workshop on Differentiable Probabilistic Robotics: Emerging Perspectives on Robot Learning*, 2023.

[22] Gareth O. Roberts and Richard L. Tweedie. Exponential convergence of langevin distributions and their discrete approximations. *Bernoulli*, 2(4):341–363, 1996.

[23] Chitwan Saharia, William Chan, Saurabh Saxena, Lala Li, Jay Whang, Emily L Denton, Kamyar Ghasemipour, Raphael Gontijo Lopes, Burcu Karagol Ayan, Tim Salimans, et al. Photorealistic text-to-image diffusion models with deep language understanding. *Advances in neural information processing systems*, 35:36479–36494, 2022.

[24] Jascha Sohl-Dickstein, Eric Weiss, Niru Maheswaranathan, and Surya Ganguli. Deep unsupervised learning using nonequilibrium thermodynamics. In *International conference on machine learning*, pages 2256–2265. PMLR, 2015.

[25] Yang Song and Stefano Ermon. Generative modeling by estimating gradients of the data distribution. *Advances in neural information processing systems*, 32, 2019.

[26] Yang Song, Jascha Sohl-Dickstein, Diederik P Kingma, Abhishek Kumar, Stefano Ermon, and Ben Poole. Score-based generative modeling through stochastic differential equations. *arXiv preprint arXiv:2011.13456*, 2020.

[27] Vikram Voleti, Alexia Jolicoeur-Martineau, and Chris Pal. Mcvd-masked conditional video diffusion for prediction, generation, and interpolation. *Advances in Neural Information Processing Systems*, 35:23371–23385, 2022.

[28] Andreas Wächter and Lorenz T Biegler. On the implementation of an interior-point filter line-search algorithm for large-scale nonlinear programming. *Mathematical programming*, 106: 25–57, 2006.

[29] Tsun-Hsuan Wang, Juntian Zheng, Pingchuan Ma, Yilun Du, Byungchul Kim, Andrew Spielberg, Joshua Tenenbaum, Chuang Gan, and Daniela Rus. Diffusebot: Breeding soft robots with physics-augmented generative diffusion models. *arXiv preprint arXiv:2311.17053*, 2023.

[30] Max Welling and Yee W Teh. Bayesian learning via stochastic gradient langevin dynamics. In *Proceedings of the 28th international conference on machine learning (ICML-11)*, pages 681–688. Citeseer, 2011.

[31] Pan Xu, Jinghui Chen, Difan Zou, and Quanquan Gu. Global convergence of langevin dynamics based algorithms for nonconvex optimization. *Advances in Neural Information Processing Systems*, 31, 2018.

[32] Ye Yuan, Jiaming Song, Umar Iqbal, Arash Vahdat, and Jan Kautz. Physdiff: Physics-guided human motion diffusion model. In *Proceedings of the IEEE/CVF International Conference on Computer Vision*, pages 16010–16021, 2023.

[33] Mingyuan Zhang, Zhongang Cai, Liang Pan, Fangzhou Hong, Xinying Guo, Lei Yang, and Ziwei Liu. Motiondiffuse: Text-driven human motion generation with diffusion model, 2022.

[34] Ziyuan Zhong, Davis Rempe, Danfei Xu, Yuxiao Chen, Sushant Veer, Tong Che, Baishakhi Ray, and Marco Pavone. Guided conditional diffusion for controllable traffic simulation. In *2023 IEEE International Conference on Robotics and Automation (ICRA)*, pages 3560–3566. IEEE, 2023.

A Broader impacts

The development of Projected Diffusion Models (PDM) may significantly enhance the application of diffusion models in fields requiring strict adherence to specific constraints and physical principles. The proposed method enables the generation of high-fidelity content that not only resembles real-world data but also complies with complex constraints, including non-convex and physical-based specifications. PDM's ability to handle diverse and challenging constraints in scientific and engineering domains, particularly in low data environments, may potentially lead to accelerating innovation and discovery in various fields.

B Expanded related work

Diffusion models with soft constraint conditioning. Variations of conditional diffusion models [13] serve as useful tools for controlling task specific outputs from generative models. These methods have demonstrated the capacity capture properties of physical design [29], positional awareness [3], and motion dynamics [32] through augmentation of these models. The properties imposed in these architectures can be viewed as soft constraints, with stochastic model outputs violating these loosely imposed boundaries.

Post-processing optimization. In settings where hard constraints are needed to provide meaningful samples, diffusion model outputs have been used as starting points for a constrained optimization algorithm. This has been explored in non-convex settings, where the starting point plays an important role in whether the optimization solver will converge to a feasible solution [21]. Other approaches have augmented the diffusion model training objective to encourage the sampling process to emulate an optimization algorithm, framing the post-processing steps as an extension of the model [10, 19]. However, an existing challenge in these approaches is the reliance on an easily expressible objective, making these approaches effective in a limited set of problems (such as the constrained trajectory experiment) while not applicable for the majority of generative tasks.

Hard constraints for generative models. Frerix et al. proposed an approach for implementing hard constraints on the outputs of autoencoders. This was achieved through scaling the generated outputs in such a way that feasibility was enforced, but the approach is to limited simple linear constraints. [17] proposed an approach to imposing constraints using "mirror mappings" with applicability exclusively to common, convex constraint sets. Due to the complexity of the constraints imposed in this paper, neither of these methods were applicable to the constraint sets explored in any of the experiments. Alternatively, work by Fishman et al. [2023, 2024] broadens the classes of constraints that can be represented but fails to demonstrate the applicability of their approach to a empirical settings similar to ours, utilizing an MLP architecture for trivial predictive tasks with constraints sets that can be represented by convex polytopes. We contrast such approaches to our work, noting that this prior work is limited to constraint sets that can be approximated by simple neighborhoods, such as an L2-ball, simplex, or polytope, whereas PDM can handle constraint sets of arbitrary complexity.

Sampling process augmentation. Motivated by the compounding of numerical error throughout the reverse diffusion process, prior work has proposed inference time operations to bound the pixel values of an image dynamically while sampling [18, 23]. Proposed methodologies have either applied reflections or simple clipping operations during the sampling process, preventing the generated image from significantly deviating from the [0,255] pixel space. Such approaches augment the sampling process in a way that mirrors our work, but these methods are solely applicable to mitigating sample drift and do not intersect our work in general constraint satisfaction.

C Preliminaries: Diffusion models

Diffusion-based generative models [14, 24] expand a data distribution, whose samples are denoted $\boldsymbol{x}_0$, through a Markov chain parameterization $\{\boldsymbol{x}_t\}_{t=1}^T$, defining a Gaussian diffusion process $p(\boldsymbol{x}_0) = \int p(\boldsymbol{x}_T) \prod_{t=1}^T p(\boldsymbol{x}_{t-1}|\boldsymbol{x}_t) d\boldsymbol{x}_{1:T}$.

In the *forward process*, the data is incrementally perturbed towards a Gaussian distribution. This process is represented by the transition kernel $q(\boldsymbol{x}_t|\boldsymbol{x}_{t-1}) = \mathcal{N}(\boldsymbol{x}_t; \sqrt{1-\beta_t}\boldsymbol{x}_{t-1}, \beta_t \boldsymbol{I})$ for some $0 < \beta_t < 1$, where the β-schedule $\{\beta_t\}_{t=1}^T$ is chosen so that the final distribution $p(\boldsymbol{x}_T)$ is nearly Gaussian. The diffusion time t allows an analytical expression for variable $\boldsymbol{x}_t$ represented by

$\chi_t(\boldsymbol{x}_0, \epsilon) = \sqrt{\alpha_t}\boldsymbol{x}_0 + \sqrt{1-\alpha_t}\epsilon$, where $\epsilon \sim \mathcal{N}(\mathbf{0}, \boldsymbol{I})$ is a noise term, and $\alpha_t = \prod_{i=1}^{t}(1-\beta_i)$. This process is used to train a neural network $\epsilon_\theta(\boldsymbol{x}_t, t)$, called the *denoiser*, which implicitly approximates the underlying data distribution by learning to remove noise added throughout the forward process.

The training objective minimizes the error between the actual noise ϵ and the predicted noise $\epsilon_\theta(\chi_t(\boldsymbol{x}_0, \epsilon), t)$ via the loss function:

$$\min_{\theta} \underset{t\sim[1,T],\, p(\boldsymbol{x}_0), \mathcal{N}(\epsilon;\mathbf{0},\boldsymbol{I})}{\mathbb{E}} \left[\|\epsilon - \epsilon_\theta(\chi_t(\boldsymbol{x}_0, \epsilon), t)\|^2 \right]. \tag{8}$$

The *reverse process* uses the trained denoiser, $\epsilon_\theta(\boldsymbol{x}_t, t)$, to convert random noise $p(\boldsymbol{x}_T)$ iteratively into realistic data from distribution $p(\boldsymbol{x}_0)$. Practically, ϵ_θ predicts a single step in the denoising process that can be used during sampling to reverse the diffusion process by approximating the transition $p(\boldsymbol{x}_{t-1}|\boldsymbol{x}_t)$ at each step t.

Score-based models [25, 26], while also operating on the principle of gradually adding and removing noise, focus on directly modeling the gradient (score) of the log probability of the data distribution at various noise levels. The score function $\nabla_{\boldsymbol{x}_t} \log p(\boldsymbol{x}_t)$ identifies the direction and magnitude of the greatest increase in data density at each noise level. The training aims to optimize a neural network $\mathbf{s}_\theta(\boldsymbol{x}_t, t)$ to approximate this score function, minimizing the difference between the estimated and true scores of the perturbed data:

$$\min_{\theta} \underset{t\sim[1,T], p(\boldsymbol{x}_0), q(\boldsymbol{x}_t|\boldsymbol{x}_0)}{\mathbb{E}} (1-\alpha_t) \left[\|\mathbf{s}_\theta(\boldsymbol{x}_t, t) - \nabla_{\boldsymbol{x}_t} \log q(\boldsymbol{x}_t|\boldsymbol{x}_0)\|^2 \right], \tag{9}$$

where $q(\boldsymbol{x}_t|\boldsymbol{x}_0) = \mathcal{N}(\boldsymbol{x}_t; \sqrt{\alpha_t}\boldsymbol{x}_0, (1-\alpha_t)\boldsymbol{I})$ defines a distribution of perturbed data $\boldsymbol{x}_t$, generated from the training data, which becomes increasingly noisy as t approach T. This paper considers score-based models.

D Effectiveness of PDM: A theoretical justification

To shed light on the PDM ability to guide the generated samples to the constrained distribution, this section provides a theoretically grounded motivation for the use of iterative projections. The analysis assumes that the feasible region $\boldsymbol{C}$ is a convex set. We start by defining the update step.

Definition D.1. The operator $\mathcal{U}$ defines a single update step for the sampling process as,

$$\mathcal{U}(\boldsymbol{x}_t^i) = \boldsymbol{x}_t^i + \gamma_t \mathbf{s}_\theta(\boldsymbol{x}_t^i, t) + \sqrt{2\gamma_t}\boldsymbol{\epsilon}. \tag{10}$$

The next result establishes a convergence criteria on the proximity to the optimum, where for each time step t there exists a minimum value of $i = \bar{I}$ such that,

$$\exists \bar{I} \ \texttt{s.t.} \ \left\| (\boldsymbol{x}_t^{\bar{I}} + \gamma_t \nabla_{\boldsymbol{x}_t^{\bar{I}}} \log q(\boldsymbol{x}_t^{\bar{I}}|\boldsymbol{x}_0)) \right\|_2 \leq \|\rho_t\|_2 \tag{11}$$

where ρ_t is the closest point to the global optimum that can be reached via a single gradient step from any point in $\mathbf{C}$.

Theorem D.2. *Let $\mathcal{P}_{\mathbf{C}}$ be a projection onto $\mathbf{C}$, $\boldsymbol{x}_t^i$ be the sample at time step $\boldsymbol{t}$ and iteration $\boldsymbol{i}$, and 'Error' be the cost of the projection (5). Assume $\nabla_{\boldsymbol{x}_t} \log p(\boldsymbol{x}_t)$ is convex. For any $\boldsymbol{i} \geq \bar{I}$,*

$$\mathbb{E}\left[\mathit{Error}(\mathcal{U}(\boldsymbol{x}_t^i), \mathbf{C})\right] \geq \mathbb{E}\left[\mathit{Error}(\mathcal{U}(\mathcal{P}_{\mathbf{C}}(\boldsymbol{x}_t^i)), \mathbf{C})\right] \tag{12}$$

The proof for Theorem D.2 is reported in §J. This result suggests that PDM's projection steps ensure the resulting samples adhere more closely to the constraints as compared to samples generated through traditional, unprojected methods. Together with the next results, it will allow us to show that PDM samples converge to the point of maximum likelihood that also satisfy the imposed constraints.

The theoretical insight provided by Theorem D.2 provides an explanation for the observed discrepancy between the constraint violations induced by the conditional model and PDM, as in Figure 1.

Corollary D.3. *For arbitrary small $\xi > 0$, there exist t and $\boldsymbol{i} \geq \bar{I}$ such that:*

$$\mathit{Error}(\mathcal{U}(\mathcal{P}_{\mathbf{C}}(\boldsymbol{x}_t^i)), \mathbf{C}) \leq \xi.$$

The above result uses the fact that the step size γ_t is strictly decreasing and converges to zero, given sufficiently large T, and that the size of each update step $\mathcal{U}$ decreases with γ_t. As the step size shrinks, the gradients and noise reduce in size. Hence, $Error(\mathcal{U}(\mathcal{P}_{\mathbf{C}}(\boldsymbol{x}_t^i))$ approaches zero with t, as illustrated in Figure 1 (right). This diminishing error implies that the projections gradually steer the sample into the feasible subdistribution of $p(\boldsymbol{x}_0)$, effectively aligning with the specified constraints.

Feasibility guarantees. PDM provides feasibility guarantees when solving convex constraints. This assurance is integral in sensitive settings, such as material analysis (Section 4.1), plausible motion synthesis (Section **??**), and physics-based simulations (Section 4.3), where strict adherence to the constraint set is necessary.

Corollary D.4. *PDM provides feasibility guarantees for convex constraint sets, for* arbitrary *density functions* $\nabla_{\boldsymbol{x}_t} \log p(\boldsymbol{x}_t)$.

E Additional results

E.1 Constrained materials morphometric parameter distributions

When analyzing both real and synthetic materials, heuristic-guided metrics are often employed to extract information about microstrucutres present in the material. When analyzing the quality of synthetic samples, the extracted data can then be used to assess how well the crystals and voids in the microstructure adhere to the training data, providing an additional qualitative metrics for analysis. To augment the metrics displayed within the body of the paper, we include here the distribution of three metrics describing these microstructures, mirroring those used by Chun et al..

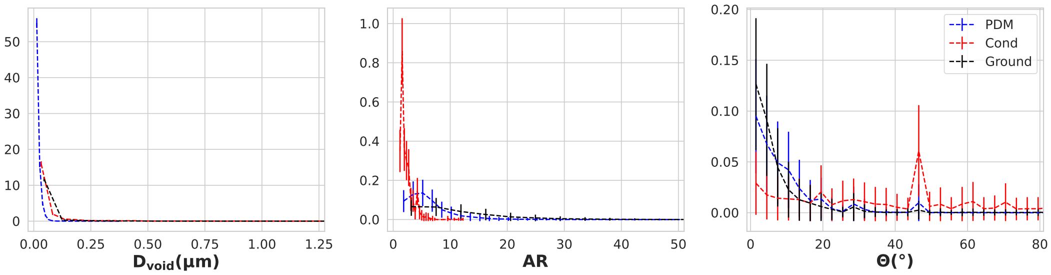

Figure 5: Distributions of the morphometric parameters, comparing the ground truth to *PDM* and *Cond* models using heuristic-based analysis.

We observe that the constraint imposition present in PDM improves the general adherence of the results to the ground truth microstructures. This suggests that the *Cond* model tends to generate to certain microstructures at a frequency that is not reflected in the training data. By imposing various porosity constraints, PDM is able to generate a more representative set of microstructures in the sampling process.

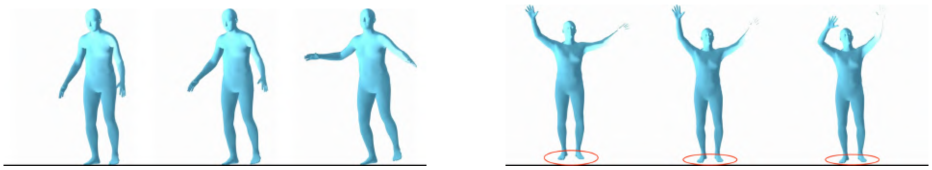

Figure 6: *PDM* (left, FID: 0.71) and conditional (*Cond*) (right, FID: 0.63) generation.

E.2 3D human motion

Here, we focus on dynamic motion generation adhering to strict physical principles using the challenging HumanML3D dataset [12]. This benchmark employs three-dimensional figures across a fourth dimension of time to simulate motion. Thus, the main challenges here are generating 3D figures **(1) including a temporal component**, while **(2) ensuring they neither penetrate the floor**

nor float in the air, as proposed by [32]. Previous studies have never achieved zero-tolerance results [32].

First, we remark that previous approaches, such as [32], relies on a computationally demanding physics simulators to transform diffusion model predictions into “physically-plausible” actions, using a motion imitation policy trained via proximal policy optimization. In contrast, and remarkably, PDM does not require such a simulator and inherently satisfies the non-penetration and non-floating constraints without external assistance, showing zero violations. For comparison, *the best outcomes reported in [32] ranged from 0.918 to 0.998 for penetration violations and 2.601 to 3.173 for floating violations* (see §E.2 for more details). Additionally, to more accurately assess the abilities of a diffusion model in the absences of physics simulator, we evaluate a conditional model with the same architecture as the PDM model, adapted from MotionDiffuse [33]. Results visualized in Figure 6 demonstrate that PDM achieves outputs on par with state-of-the-art FID scores.

We highlight that unlike the approach proposed by [32], our approach guarantees the generated motion does not violate the penetrate and float constraints. The results are tabulated in Table 1 (left) and report the violations in terms of measured distance the figure is either below (penetrate) or above (float) the floor. For comparison, we include the projection schedules utilized by PhysDiff which report the best results to show that even in these cases the model exhibits error.

Method	**FID**	**Penetrate**	**Float**
PhysDiff [32] (Start 3, End 1)	0.51	0.918	3.173
PhysDiff [32] (End 4, Space 1)	**0.43**	0.998	2.601
PDM	0.71	**0.00**	**0.00**

Table 1: PDM performance compared to (best) PhysDiff results on HumanML3D.

The implementation described by [32] applies a physics simulator at scheduled intervals during the sampling process to map the diffusion models prediction to a “physically-plausible action that imitates data points of the training distribution. This simulator dramatically alters the diffusion models outputs utilizing a learned motion imitation policy, which has been trained to match the ground truth samples using proximal policy optimization. In this setting the diffusion model provides a starting point for the physics simulator and is not directly responsible for the final results of these predictions. Direct parallels can be drawn between this approach and other methods which solely task the diffusion model with initializing an external model [10, 21]. Additionally, while the authors characterize this mapping as a projection, it is critical to note that this is a projection onto the learned distribution of the simulator and not a projection onto a feasible set, explaining the remaining constraint violations in the outputs.

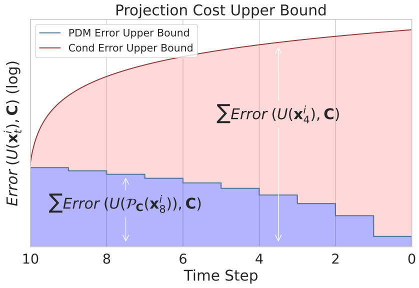

Figure 7: Visualization of the decreasing upper bound on error introduced in a single sampling step for *PDM*, as opposed to the strictly increasing upper bound of conditional (*Cond*) models.

E.3 Convergence of PDM

As shown in Figure 1, the PDM sampling process converges to a feasible subdistribution, a behavior that is generally not present in standard conditional models. Corollary D.3 provides insight into this behavior as it outlines the decreasing upper bound on *‘Error’* that can be introduced in a single sampling step. To further illustrate this behavior, the decreasing upper bound can be illustrated in Figure 7.

F Experimental settings

In the following section, further details are provided as to the implementations of the experimental settings used in this paper.

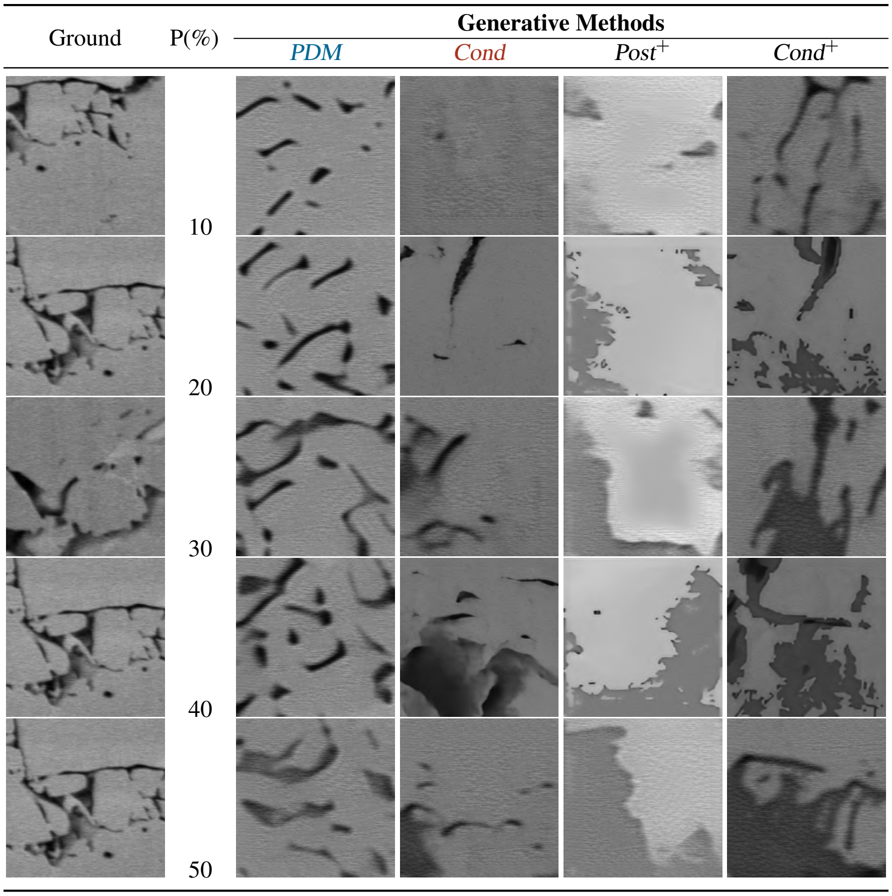

Figure 8: Porosity constrained microstructure visualization at varying of the imposed porosity constraint amounts (expanded from Figure 2).

F.1 Constrained materials

Microstructures are pivotal in determining material properties. Current practice relies on physics-based simulations conducted upon imaged microstructures to quantify intricate structure-property linkages [4]. However, acquiring real material microstructure images is both costly and time-consuming, lacking control over attributes like porosity, crystal sizes, and volume fraction, thus necessitating "cut-and-try" experiments. Hence, the capability to generate realistic synthetic material microstructures with controlled morphological parameters can significantly expedite the discovery of structure-property linkages.

Previous work has shown that conditional generative adversarial networks (GAN) [11] can be used for this end [5], but these studies have been unable to impose verifiable constraints on the satisfaction of these desired properties. To provide a conditional baseline, we implement a conditional DDPM modeled after the conditional GAN used by Chun et al. with porosity measurements used to condition the sampling.

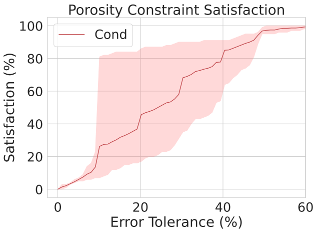

Figure 9: Conditional diffusion model (*Cond*): Frequency of porosity constraint satisfaction (y-axis) within an error tolerance (x-axis) over 100 runs.

Projections. The porosity of an image is represented by the number of pixels in the image which are classified as damaged regions of the microstructure. Provided that the image pixel intensities are scaled to [-1, 1], a threshold is set at zero, with pixel intensities below this threshold being classified as damage regions. To project, we implement a top-k algorithm that leaves the lowest and highest intensity pixels unchanged, while adjusting the pixels nearest to the threshold such that the total number of pixels below the threshold precisely satisfies the constraint.

Conditioning. The conditional baseline is conditioned on the porosity values of the training samples. The implementation of this model is as described by Ho and Salimans.

Original training data. We include samples from the original training data to visually illustrate how closely our results perform compared to the real images. As the specific porosities we tested on are not adhered to in the dataset, we illustrate this here as opposed to in the body of the text.

We observe that only the Conditional model and PDM synthesize images that visually adhere to the distribution, while post-processing methods do not provide adequate results for this complex setting.

F.2 3D human motion

Projections. The penetration and floatation constraints can be handled by ensuring that the lowest point on the z-axis is equal to the floor height. Additionally, to control the realism of the generated figures, we impose equality constraints on the size of various body parts, including the lengths of the torso and appendages. These constraints can be implemented directly through projection operators.

Conditioning. The model is directly conditioned on text captions from the HumanML3D dataset. The implementation is as described in [33].

F.3 Constrained trajectories

To circumvent the challenge of guaranteeing collision-free paths, previous methods have relied on sampling large batches of trajectories, selecting a feasible solution if available [3]. We use the state-of-the-art *Motion Planning Diffusion* [3] as a conditional model baseline for this experiment and the associated datasets to train each of the models. For the *Cond*$^+$ model, we emulate the approach proposed by [21], using the conditional diffusion model to generate initial points for an optimization solver. In this setting, the projection operator used by PDM is non-convex, and the implementation uses an interior point method [28]. While the feasible region is non-convex, our approach *never report unfeasible solutions* as the distance from the learned distribution decreases, unlike other methods. In contrast, using the same method for a single post-processing projection (*Post*$^+$) does not enhance the feasibility of solutions compared to the unconstrained conditional model (*Cond*), highlighting the limitations of these single corrections in managing local infeasibilities. These observations are consistent with the analysis of Figure 1.

Projections. For this experiment, we represent constraints such that the predicted path avoids intersecting the obstacles present in the topography. These are parameterized to a non-convex interior point method solver. For circular obstacles, this can be represented by a minimum distance requirement, the circle radius, imposed on the nearest point to the center falling on a line between p_n and p_{n+1}. These constraints are imposed for all line segments. We adapt a similar approach for non-circular obstacles by composing these of multiple circular constraints, hence, avoiding over-constraining the problem. More customized constraints could be implement to better represent the feasible region, likely resulting in shorter path lengths, but these were not explored for this paper.

Conditioning. The positioning of the obstacles in the topography are passed into the model as a vector when conditioning the model for sampling. Further details can be found the work presented by Carvalho et al., from which this baseline was directly adapted.

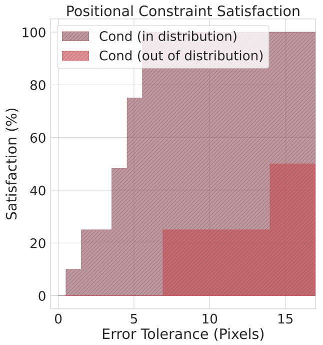

Figure 10: Conditional diffusion model (*Cond*): Frequency of constraint satisfaction (y-axis) given an error tolerance (x-axis) over 100 runs.

F.4 Physics-informed motion

The dataset is generated with object starting points sampled uniformly in the interval [0, 63]. For each data point, six frames are

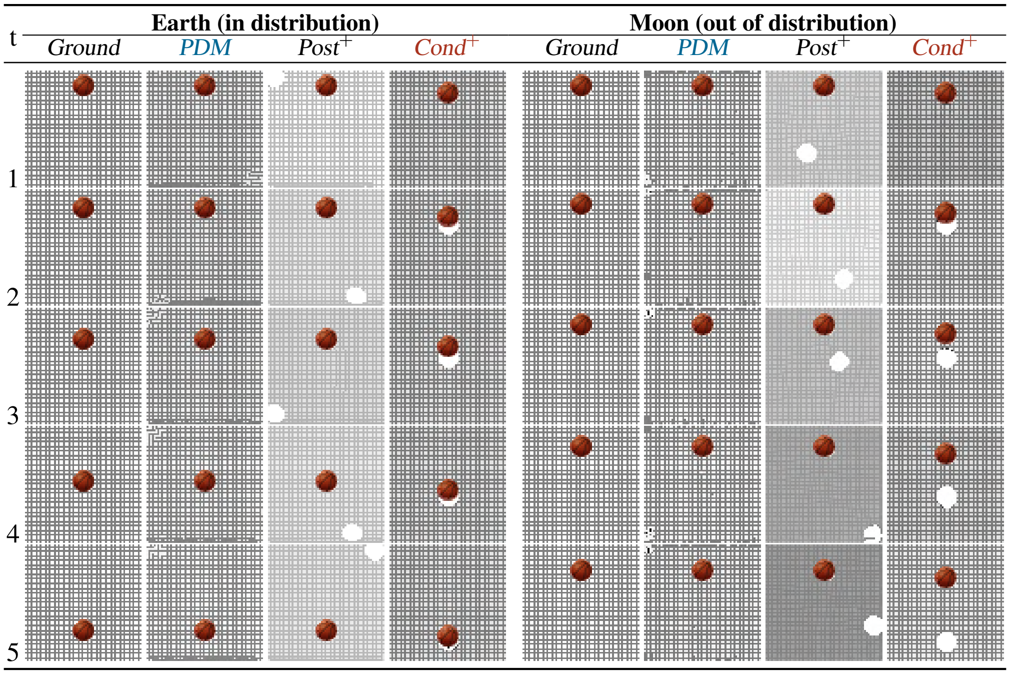

Figure 11: Sequential stages of the physics-informed models for in-distribution (Earth) and out-of-distribution (Moon) constraint imposition.

included with the position changing as defined in Equation 7 and the initial velocity $\mathbf{v}_0 = 0$. Pixel values are scaled to [-1, 1]. The diffusion models are trained on 1000 points with a 90/10 train/test split.

Projections. Projecting onto positional constraints requires a two-step process. First, the current position of the object is identified and all the pixels that make up the object are set to the highest pixel intensity (white), removing the object from the original position. The set of pixel indices representing the original object structure are stored for the subsequent step. Next, the object is moved to the correct position, as computed by the constraints, as each pixel from the original structure is placed onto the center point of the true position. Hence, when the frame is feasible prior to the projection, the image is returned unchanged, which is consistent with the definition of a projection.

Conditioning. For this setting, the conditional video diffusion model takes two ground truth frames as inputs, from which it infers the trajectory of the object and the starting position. The model architecture is otherwise as specified by Voleti et al..

G PDM for score-based generative modeling through stochastic differential equations

G.1 Algorithms

While the majority of our analysis focused on the developing these techniques to the sampling architecture proposed for Noise Conditioned Score Networks [25], this approach can directly be adapted to the diffusion model variant Score-Based Generative Modeling with Stochastic Differential Equations proposed by Song et al. Although our observations suggested that optimizing across a continuum of distributions resulted in less stability in diverse experimental settings, we find that this method is still effective in producing high-quality constrained samples in others.

We included an updated version of Algorithm 1 adapted to these architectures.

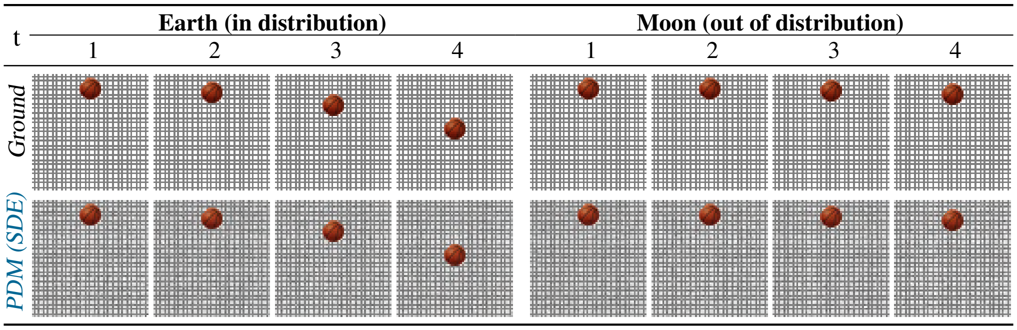

Figure 12: Sequential stages of the physics-informed models for in-distribution (Earth) and out-of-distribution (Moon) constraint imposition via Score-Based Generative Modeling with SDEs.

Algorithm 2: PDM Corrector Algorithm

```
$\mathbf{x}_N^0 \sim \mathcal{N}(\mathbf{0}, \sigma_{\max}^2 \mathbf{I})$
for $t \leftarrow T$ to $1$ do
    for $i \leftarrow 1$ to $M$ do
        $\epsilon \sim \mathcal{N}(\mathbf{0}, \mathbf{I})$
        $\mathbf{g} \leftarrow \mathbf{s}_{\theta *}(\mathbf{x}_t^{i-1}, \sigma_t)$
        $\gamma \leftarrow 2(r||\epsilon||_2/||\mathbf{g}||_2)^2$
        $\mathbf{x}_t^i \leftarrow \mathcal{P}_{\mathbf{C}}(\mathbf{x}_t^{i-1} + \gamma \mathbf{g} + \sqrt{2\gamma}\epsilon)$
    $\mathbf{x}_{t-1}^0 \leftarrow \mathbf{x}_t^M$
return $\mathrm{x}_0^0$
```

We note that a primary discrepancy between this algorithm and the one presented in Section 3.2 is the difference in γ. As the step size is not strictly decreasing, the guidance effect provided by PDM is impacted as Corollary D.3 does not hold for this approach. Hence, we do not focus on this architecture for our primary analysis, instead providing supplementary results in the subsequent section.

G.2 Results

We provide additional results using the Score-Based Generative Modeling with Stochastic Differential Equations. This model produced highly performative results for the Physics-informed Motion experiment, with visualisations included in Figure 12. This model averages an impressive inception score of **24.2** on this experiment, slightly outperforming the PDM implementation for Noise Conditioned Score Networks. Furthermore, it is equally capable in generalizing to constraints that were not present in the training distribution.

H Computational costs

To compare the computational costs of sampling with PDM to our baselines, we record the execution times for the reverse process of a single sample. *The implementations of PDM have not been optimized for runtime, and represent an upper bound.* All sampling is run on two NVIDIA A100 GPUs. All computations are conducted on these GPUs with the exception of the interior point method projection used in the 3D Human motion experiment and the Constrained Trajectories experiment which runs on two CPU cores.

We implement projections at all time steps in this analysis, although practically this is can be optimized to reduce the total number of projections as described in the subsequent section. Additionally, we set $M = 100$ and $T = 10$ for each experiment. The increase in computational cost present in PDM is directly dependant on the tractability of the projections and the size of M.

	Constrained Materials	3D Human Motion	Constrained Trajectories	Physics-informed Motion
PDM	26.89	682.40*	383.40*	48.85
Post$^+$	26.01	–	–	27.58
Cond	18.51	13.79	0.56	35.30
Cond$^+$	18.54	–	106.41	36.63

Table 2: Average sampling run-time in seconds.

The computational cost of the projections is largely problem dependant, and we conjecture that these times could be improved by implementing more efficient projections. For example, the projection for Constrained Trajectories could be dramatically improved by implementing this method on the GPUs instead of CPUs (*). However, these improvements are beyond the scope of this paper. Our projection implementations are further described in §F.

Additionally, the number of iterations for each t can often be decreased below $M = 100$ or the projection frequency can be adjusted (as has been done for in this section for the CPU implemented projections), offering additional speed-up.

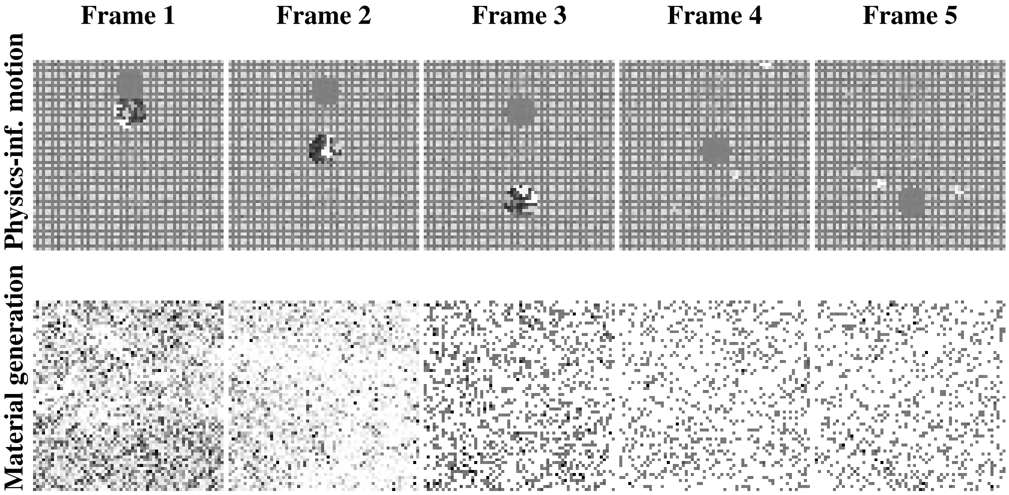

Figure 13: Iterative projections using model trained with variational lower bound objective.

I Variational lower bound training objective

As defined in Equation 2, PDM uses a score-matching objective to learn to the gradients of the log probability of the data distribution. This understanding allows the sampling process to be framed in a light that is consistent to optimization theory, allowing equivalences to be drawn between the proposed sampling procedure and projected gradient descent.

Other DDPM and DDIM implementation utilize a variation lower bound objective, which is a tractable approach to minimizing the negative log likelihood on the network's noise predictions. While this approach was inspired by the score-matching objective, we empirically demonstrate that iterative projections perform much worse in our tested settings than models optimized using this training objective, producing clearly inferior solutions in the Physics-informed experiments and failing to produce viable solutions in the material science domain explored.

This approach (visualized in Figure 13) resulted in an FID score of 113.8 ± 4.9 on the Physics-informed Motion experiment and 388.2 ± 13.0 on the Constrained Materials experiment, much higher than those produced using the score-matching objective, adopted in our paper. We hold that this is because the approach proposed in our paper is more theoretically sound when framed in terms of a gradient-based sampling process.

J Missing proofs

Proof of Theorem D.2

Proof. By optimization theory of convergence in a convex setting, provided an arbitrarily large number of update steps M, $\boldsymbol{x}_t^M$ will reach the global minimum. Hence, this justifies the existence of $\bar{I}$ as at some iteration as $i \to \infty$, $\left\|\boldsymbol{x}_t^i + \gamma_t \nabla_{\boldsymbol{x}_t^i} \log q(\boldsymbol{x}_t^i|\boldsymbol{x}_0)\right\|_2 \leq \|\rho_t\|_2$ will hold for every iteration thereafter.

Consider that a gradient step is taken without the addition of noise, and $i \geq \bar{I}$. Provided this, there are two possible cases.

Case 1: Assume $\boldsymbol{x}_t^i + \gamma_t \nabla_{\boldsymbol{x}_t^i} \log q(\boldsymbol{x}_t^i|\boldsymbol{x}_0)$ is closer to the optimum than ρ_t. Then, $\boldsymbol{x}_t^i$ is infeasible.

This claim is true by the definition of ρ_t, as $\boldsymbol{x}_t^i + \gamma_t \nabla_{\boldsymbol{x}_t^i} \log q(\boldsymbol{x}_t^i|\boldsymbol{x}_0)$ is closer to μ than is achievable from the nearest feasible point to μ. Hence, $\boldsymbol{x}_t^i$ must be infeasible.

Furthermore, the additional gradient step produces a point that is closer to the optimum than possible by a single update step from the feasible region. Hence it holds that

$$\mathit{Error}(\boldsymbol{x}_t^i + \gamma_t \nabla_{\boldsymbol{x}_t^i} \log q(\boldsymbol{x}_t^i|\boldsymbol{x}_0)) > \mathit{Error}(\mathcal{P}_{\mathbf{C}}(\boldsymbol{x}_t^i) + \gamma_t \nabla_{\mathcal{P}_{\mathbf{C}}(\boldsymbol{x}_t^i)} \log q(\mathcal{P}_{\mathbf{C}}(\boldsymbol{x}_t^i)|\boldsymbol{x}_0)) \tag{13}$$

as the distance from the feasible region to the projected point will be at most the distance to ρ_t. As this point is closer to the global optimum than ρ_t, the cost of projecting $\boldsymbol{x}_t^i + \gamma_t \nabla_{\boldsymbol{x}_t^i} \log q(\boldsymbol{x}_t^i|\boldsymbol{x}_0)$ is greater than that of any point that begins in the feasible region.

Case 2: Assume $\boldsymbol{x}_t^i + \gamma_t \nabla_{\boldsymbol{x}_t^i} \log q(\boldsymbol{x}_t^i|\boldsymbol{x}_0)$ is equally close to the optimum as ρ_t. In this case, there are two possibilities; either (1) $\boldsymbol{x}_t^i$ is the closest point in $\mathbf{C}$ to μ or (2) $\boldsymbol{x}_t^i$ is infeasible.

If the former is true, $\boldsymbol{x}_t^i = \mathcal{P}_{\mathbf{C}}(\boldsymbol{x}_t^i)$, implying

$$\mathit{Error}(\boldsymbol{x}_t^i + \gamma_t \nabla_{\boldsymbol{x}_t^i} \log q(\boldsymbol{x}_t^i|\boldsymbol{x}_0)) = \mathit{Error}(\mathcal{P}_{\mathbf{C}}(\boldsymbol{x}_t^i) + \gamma_t \nabla_{\mathcal{P}_{\mathbf{C}}(\boldsymbol{x}_t^i)} \log q(\mathcal{P}_{\mathbf{C}}(\boldsymbol{x}_t^i)|\boldsymbol{x}_0)) \tag{14}$$

Next, consider that the latter is true. If $\boldsymbol{x}_t^i$ is not the closest point in $\mathbf{C}$ to the global minimum, then it must be an equally close point to μ that falls outside the feasible region. Now, a subsequent gradient step of $\boldsymbol{x}_t^i$ will be the same length as a gradient step from the closest feasible point to μ, by our assumption.

Since the feasible region and the objective function are convex, this forms a triangle inequality, such that the cost of this projection is greater than the size of the gradient step. Thus, by this inequality, Equation 13 applies.

Finally, for both cases we must consider the addition of stochastic noise. As this noise is sampled from the Gaussian with a mean of zero, we synthesize this update step as the expectation over,

$$\mathbb{E}\left[\mathit{Error}(\boldsymbol{x}_t^i + \gamma_t \nabla_{\boldsymbol{x}_t^i} \log q(\boldsymbol{x}_t^i|\boldsymbol{x}_0) + \sqrt{2\gamma_t}\boldsymbol{\epsilon})\right] \geq \mathbb{E}\left[\mathit{Error}(\mathcal{P}_{\mathbf{C}}(\boldsymbol{x}_t^i) + \gamma_t \nabla_{\mathcal{P}_{\mathbf{C}}(\boldsymbol{x}_t^i)} \log q(\mathcal{P}_{\mathbf{C}}(\boldsymbol{x}_t^i)|\boldsymbol{x}_0) + \sqrt{2\gamma_t}\boldsymbol{\epsilon})\right] \tag{15}$$

or equivalently as represented in Equation 12.

□